Shape-Based Kidney Detection and Segmentation in Three-Dimensional Abdominal Ultrasound Images

Mahdi Marsousi[1], Konstantinos N. Plataniotis[2] and Stergios Stergiopoulos[3]

***Abstract*— Due to recent technical advancements of three-dimensional ultrasound imaging systems, applications of this imaging modality have been expanding from the fetal imaging to cardiac- and abdominal-diagnosis. Among all internal organs, diagnosing the kidney has a paramount importance for rapid bedside treatment of trauma and kidney stone patients using ultrasound images. Although three-dimensional ultrasound provides higher level of structural information of kidneys, manual kidney diagnosis using three-dimensional ultrasound images requires a highly trained medical staff, due to the extensive visual complexity which three-dimensional images contain. Therefore, computer aided automated kidney diagnosis becomes very essential. Due to the challenging problems of ultrasound images, such as speckle noise and inhomogeneous intensity profile, kidney segmentation in three-dimensional ultrasound images has not been sufficiently investigated by researchers. In this paper, we first propose a new automated kidney detection approach using three-dimensional Morison's pouch ultrasound images. Then, we proposed a shape-based method to segment the detected kidneys. A preprocessing step is utilized to overcome the ultrasound challenges. Based on a set of 14 ultrasound volumes, we have evaluated the detection rate of our proposed kidney detection approach which is 92.86%. For kidney segmentation, we compared our proposed method with an existing approach, and the performed statistical analysis strongly validates the superiority of our proposed method with $p = 0.000032$.**

I. INTRODUCTION

Thanks to the recent technological advancements in three-dimensional (3-D) ultrasound imaging, and also under development innovations in 3-D ultrasound beam-forming [1][2][3][4], 3-D ultrasound imaging is expanding its medical applications beyond what has been conceived a few years ago [5]. There are some reasons to use ultrasound: (1) unlike Computed Tomography (CT) and Magnetic Resonance Imaging (MRI), ultrasound imaging is non-invasive and does not impose any restrictions on the use to patients; (2) Since it is portable, unstable patients are not required to be moved from a place with resuscitation facilities to another place for imaging, unlike CT and MRI; (3) Compared to CT and MRI, 3-D ultrasound provides real-time imaging. In 3-D ultrasound, the location of the ultrasound signal in 3-D space is known. This provides a volumetric representation of internal organs, which could not be achieved with 2-D B-scan ultrasound images [6]. 3-D ultrasound imaging also provides some other advantages: (1) Using 3-D ultrasound, new images are visualized, which otherwise, a clinician should mentally build it up from two-dimensional (2-D) ultrasound images; (2) 3-D ultrasound provides more accurate quantitative assessment of volumes by eliminating geometric estimations like the ellipsoid based formula [6].

Kidney diagnosis using 3-D ultrasound has a vital significance in some medical applications. Kidney is visible in abdominal Sonography, specifically in the Morison's pouch view. A computer aided diagnosis of the kidney can be used on 3-D ultrasound volume of the Morison's pouch view for detecting trauma and kidney stone patients. Trauma is a free fluid region caused by an internal bleeding, and appears as a dark (low echoic) region [7]. Abdominal trauma is usually located around the upper boundary of the kidney [8], and thus, kidney detection is required as an important step for trauma diagnosis. Since kidney stones highly scatter ultrasound beams, they cause dark shadows in kidney images, which can be characterized to detect kidney stones.

The kidney has a unique structure in 3-D ultrasound images which makes it distinguishable from all other abdominal organs. However, there are some challenges toward kidney detection: (1) speckle noise is caused by the nature of the ultrasound imaging, which results in having low qualities in ultrasound images [9]; (2) there exist gaps among the kidney boundary [10]; (3) kidney stones create shadows, which partially occlude the kidney shape; (4) because of the ultrasound probe miss-alignment, the kidney shape is not fully visible. Due to these challenges, kidney segmentation using 3-D ultrasound images has not been thoroughly investigated.

Kidney segmentation has been extensively investigated in CT and MRI images such as: Tsagaan et al. (2001) [11], Tsagaan et al. (2002) [12], Lin et al. (2006) [13], Chen and Bagci (2011) [14], Li and Fei (2008) [15], Khalifa et al. (2011) [16] and Akbari et al. (2012) [17]. Kidney segmentation using ultrasound images has been investigated by Fernandez and Lopez (2005) [18], and Prevost et al. (2011) [19]. Fernandez and Lopez (2005) [18] proposed a method to segment the kidney boundary in 3-D ultrasound images, which applies Markov random field and active contours (MRF-AC). This work performs 2-D segmentation to outline kidney boundaries on each ultrasound slice, and then combines segmented contours in all slices to reconstruct a 3-D kidney shape. This approach requires an user intervention to adjust the kidney shape in a single slice of the 3-D volume, and therefore, it is a semi-automated

[1] M. Marsousi is with the Multimedia Processing Lab in the communication group of the Electrical and Computer Engineering department at the University of Toronto marsousi@comm.utoronto.ca

[2] K. Plataniotis is with the Electrical and Computer Engineering department, University of Toronto kostas@ece.utoronto.ca

[3] S. Stergopoulos is with the Defence Research and Development Canada Toronto, an Agency for the Candadian department of defence. stergio.stergiopoulos@drdc-rddc.gc.ca

978-1-4244-7929-0/14/$26.00 ©2014 IEEE

approach. In another work, Prevost et al. (2011) [19] applied the three-dimensional contrast enhanced ultrasound images in which the kidney appears brighter than other regions. In this method, a 3-D deformable model is applied which supports both global and local deformations. As the main contribution of this work, user intervention, which is a set of manual landmarks inside or/and outside kidneys, are directly imposed on the energy functional to improve the kidney segmentation accuracy. The success rate of this approach depends on the contrast enhanced ultrasound images, and its performance in 3-D ultrasound images has not been reported. In addition, this approach does not provide fully-automated kidney segmentation.

In this paper, we propose a new approach to detect and segment kidneys in 3-D ultrasound images. We incorporate our prior knowledge on kidney shapes variability to generate a probabilistic kidney shape model (PKSM). This model maps voxels on a 3-D grid into a scalar value which represent the probability of being inside the kidney. In the kidney detection step, we perform a fast preprocessing to generate a binarized volume, and then we use PKSM to search using the 3-D correlation for the best matching position in the volume, and then, we decide whether a kidney exist or not. In the next step, we first perform a more demanding preprocessing to de-speckle an input volume, and then, we use PKSM to initialize a deformable model on the detected kidney position. Afterward, we apply a global deformation to fit the kidney shape model inside the ultrasound volume, and then, a level-set propagation is engaged to finely outline the kidney shape. The rest of the paper is organized as follows: In section II, we briefly represent our proposed approach. In section III, we provide evaluation results, and compare our method with an existing approach. In section IV, we discuss results and perform a conclusion.

II. The Proposed Method

A. Problem Definition

Lets define $V \in \Re^{N_x \times N_y \times N_z}$ is a 3-D ultrasound image which maps a voxel in a 3-D grid into a scalar value representing an intensity level, $V(n,m,k) \in [0,1,\cdots,255]$ where $n \in [1,\cdots,N_x]$, $m \in [1,\cdots,N_y]$, and $k \in [1,\cdots,N_z]$. For each 3-D ultrasound volume with a kidney, V^i, a binarized mask, $B^i \in \Re^{N_x \times N_y \times N_z}$, is manually drawn which is 1 for voxels belonging to the kidney, and 0 elsewhere. The binarized volumes are used for generating PKSM, and for evaluating the kidney segmentation accuracy. We define two problems to be addressed in this paper: (1) decide whether an input 3-D ultrasound image contains a kidney, and if it exists, where is it located; (2) segment the detected kidney. Since the proposed approach will be used in an online processing scheme [20], kidney detection should be both fast and accurate. When, the correct view with a kidney is detected, the kidney should be very accurately segmented, and its computational time must not be a concern. The proposed processing pipeline is designed to observe the above-mentioned concerns.

B. Generating Probabilistic Kidney Shape Model

Since kidney shapes are highly variable, a probabilistic model is required to cover a variety of upcoming kidneys. We define the probabilistic template as, $Tmp \in \Re^{N_x^{Tmp} \times N_y^{Tmp} \times N_z^{Tmp}}$, where $0 \leq Tmp(x,y,z) \leq 1$. A subset of binarized masks are selected, $B^i \in \Re^{N_x^i \times N_y^i \times N_z^i}$ and $i \in U_{tmp}$. An arbitrary B^{i^*}, where $i^* \in U_{tmp}$, is selected to create the initial Tmp. Then, other binarized masks, $i \in U_{tmp}$, are registered on Tmp, using the rigid-body registration [21], aiming to remove the dependency of Tmp on miss-alignments of binarized volumes. Therefore, Tmp will only carry information of the kidney shape variability. Our probabilistic model only relies on the mean. The block diagram of generating PKSM is shown in Fig. 1.

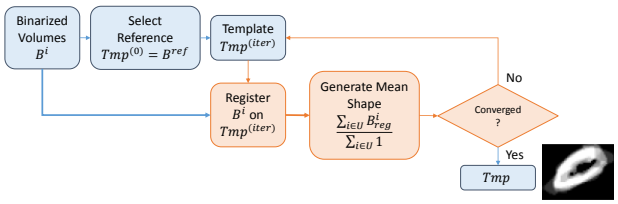

Fig. 1. Displaying the block diagram of generating the probabilistic kidney shape model.

C. Kidney Detection

As discussed in subsection II-A, kidney detection should be fast enough to be adopted in an online process. Thus, to reduce the computational cost, our proposed kidney detection is performed in half-scale. The half size volume, V^i_{hf}, is generated using linear interpolation.

In the next step, two processing blocks are added to overcome ultrasound images including speckle noise and low contrast. To reduce speckle noise, a 3-D finite impulse response (FIR) filter, which is a multiplication of a zero mean 3-D Gaussian function and the Hamming window, is used, and the resultant volume is V^i_{dn}. N_{GH} is the width of Gaussian-Hamming filter [20]. The Gaussian filter is both separable and isotropic, and therefore reduces the 3-D filtering task into three one-dimensional convolutions. The Hamming window is utilized to produce the FIR filter because it minimizes the maximum side lobe.

The denoised volume, V^i_{dn}, still suffers from a low contrast intensity profile. This histogram inefficiency results in an insufficient difference between intensity profiles of the kidney and its surrounding voxels, which may cause to fail kidney detection. The remedy of this problem is to apply histogram equalization. In histogram equalization, a transformation function is defined based on the cumulative density function (CDF), which transforms histogram regions with high concentration into wider regions, while other histogram regions are transformed into narrower regions [22]. Histogram equalization operates as a global transformation, and is not able to capture local intensity conditions of the entire image. The solution to this problem is localized histogram equalization which operates on localized intensity

profiles [23]. In the localized histogram equalization, for each voxel in the volume, $V^i_{dn}(n,m,k)$, a block of neighbor voxels is selected as, $N(n,m,k) = \{V^i_{dn}(n+x', m+y', k+z') | x', y', z' \in \{-N_L, \ldots, N_L\}\}$. N_L is the width of the neighbor block. Then, histogram equalization is applied on $N(n,m,k)$, and the equalized intensity level of the center point is taken as, $V^i_{Eq}(n,m,k)$. Since this method independently calculates the transformation function for each voxel, its computational cost is high. Our observation shows that a good trade off between the quality and computational cost is achieved by selecting $N_L = 11$.

In the next step, the equalized volume, V^i_{Eq}, is segmented into two regions: dark and bright. Kidney voxels are dark, while surrounding voxels of kidney are brighter. Due to inconsistent intensity profile of internal tissues throughout an ultrasound volume, using a global threshold for the entire volume might not be useful. Therefore, we selected the ordinary Kriging approach, which is a local thresholding method [24]. This method utilizes spatial covariance and indicator Kriging to locally segment voxels into dark and bright regions. The output of ordinary Kriging segmentation is a binarized volume, V^i_{Bin}, which values 0 and 1 correspond to non-kidney and kidney voxels, respectively.

The main step of the proposed kidney detection algorithm is to search for a kidney shape in the binarized volume, V^i_{Bin}. This is performed based on the prior knowledge of the kidney shape. PKSM is used as a 3-D template to find the maximum matching voxel based on the 3-D correlation, as a potential kidney. The value corresponding to the maximum matching voxel is compared with a threshold value, th_{KD}, to decide whether a kidney exists or not. If the maximum correlation is greater than th_{KD}, the position of the potential kidney is selected as a detected kidney position, $\vec{P}_{DK}$. The value of the threshold is set to $th_{KD} = 3000$ to maximize the number of true-positives detections (T-P) and true-negatives (T-N) detections in our ultrasound volume database. The processing pipeline of the proposed kidney detection method is shown in Fig. 2.

D. Kidney Segmentation

The key idea of our proposed kidney segmentation is to use PKSM to initiate the segmentation. Then we apply an affine deformation to fit PKSM into the kidney in the ultrasound volume. Using this step, the kidney segmentation method is initiated closer to the actual kidney boundaries, and as a result, kidney segmentation is improved because,

1) kidney segmentation requires less efforts to converge into the final segmentation result, and therefore it spends less computations;
2) kidney segmentation is a non-rigid deformation, and therefore, it is prone to leak into gaps within kidneys' boundaries, and using the improved initialization, the chance of leaking into non-kidney regions is minimized.

The fitted PKSM is used to initialize level-set function. Then, a level-set propagation is applied as a non-rigid deformation to finely segment a kidney. Our proposed kidney segmentation combines rigid and non-rigid deformations (Fig. 3).

Ultrasound volumes are contaminated by multiplicative noise, also known as speckle noise [9]. Our goal is to reduce the speckle noise while preserving the kidney shape. The anisotropic diffusion filter (ADF) [9] has shown to be a useful method to de-speckle our 3-D ultrasound images. It strongly filters an image in regions away from object boundaries to suppress speckle noise. In regions close to kidney boundaries, ADF performs smoothing in the parallel direction to the object boundaries. Therefore, it not-only preserves edges, but also emphasizes edge information. Since speckle reduction anisotropic diffusion is an iterative process, it is computationally demanding, and therefore, it is only used in the kidney segmentation step, but not for kidney detection.

The initialization step of kidney segmentation has a great impact on the final segmentation result. A good initialization is required (1) to avoid segmentation to trap in a local minima, and (2) to reduce the convergence time of kidney segmentation. We first align PKSM on $\vec{P}_{DK}$ in the ultrasound volume, and generate a new volume, $V^i_\phi \in \Re^{N_x \times N_y \times N_z}$. Then, a rigid-body deformation based on affine transformation is applied on V^i_ϕ to maximize the fitness of PKSM on the kidney inside the ultrasound volume [21]. Using a rigid-body deformation, the speed of kidney segmentation is increased since less non-rigid deformation, which is more computationally demanding, is required.

After performing the rigid-body deformation, we are ready to initialize the level-set segmentation. We define a level-set function as, $\phi(\vec{P}, t)$, where $\vec{P} \in \Re^3$ and t represents the temporal domain. Therefore, $\phi(\vec{P}, t)$, maps a point in a four-dimensional space into a one-dimensional space, $\phi : \Re^4 \rightarrow \Re$. The initial level-set function is $\phi(\vec{P}, t=0) = \phi_0(\vec{(P)})$, and is set in our framework as follows,

$$\phi_0(\vec{P}) = \begin{cases} -1 & \hat{V}^i_\phi(\vec{P}) = 0 \\ 1 & \hat{V}^i_\phi(\vec{P}) > 0 \end{cases} . \tag{1}$$

Afterward, we apply the level-set propagation based on the regional information [25], which is also known as the region-based active contour, to segment the kidney. Compared to edge-based deformable model, the region-based approach is less sensitive to noise and weak edges. Let Ω be a bounded open subset of $\Re^3$, and $V^i : \Omega \mapsto \Re$ is a 3-D ultrasound image, and ϕ is the initialized level-set function. The general expression of the energy functional for region-based level-set is formulated as follows,

$$\begin{aligned} J(\phi) = \nu_{in} &\int_\Omega g_{in}(\mathbf{x}, \phi(\mathbf{x})) H(\phi(\mathbf{x})) dxdydz \\ &+ \nu_{out} \int_\Omega g_{out}(\mathbf{x}, \phi(\mathbf{x}))(1 - H(\phi(\mathbf{x}))) dxdydz \\ &+ \nu_c \int_\Omega g_c(\mathbf{x}, \phi(\mathbf{x})) \delta(\phi(\mathbf{x})) \left\| \nabla \phi(\mathbf{x}) \right\| dxdydz, \end{aligned} \tag{2}$$

where the first and second terms are energy terms related to the inside and outside regions of the segmentation surface,

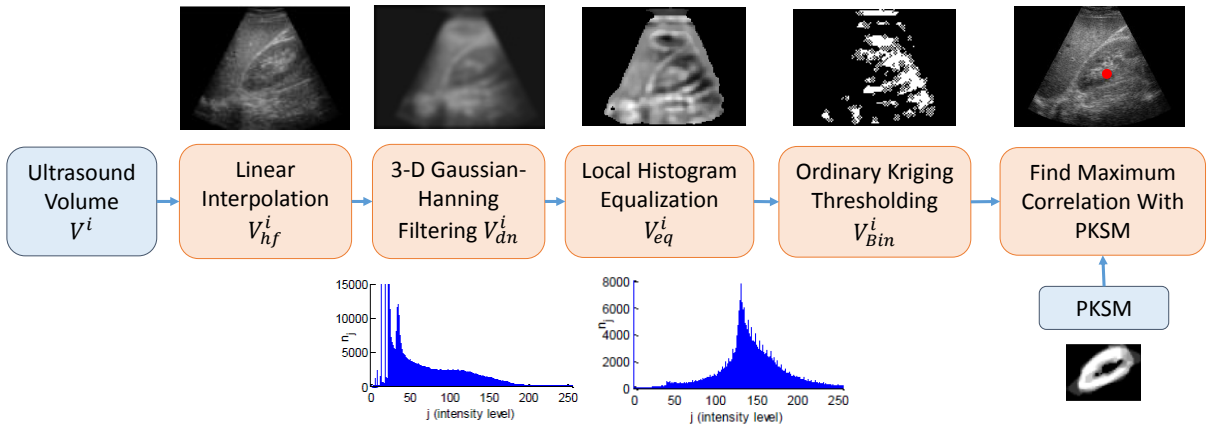

Fig. 2. Displaying the block diagram of our proposed kidney detection. The bottom left nad bottom right histograms belong to the de-speckled volume and equalized volume, respectively. The red circle in the top right image shows the detected kidney position.

respectively. The last term relates to the voxels which are located on the segmentation surface. Also, $g_{in}(.)$, $g_{out}(.)$ and $g_c(.)$ are functions of intensity levels of voxels in object, background and over the contour. ν_{in}, ν_{out} and ν_c are regulation parameters which control the influence of each energy term in the surface evolution. $H(.)$ and $\delta(.)$ are Heaviside and Dirac functions [25].

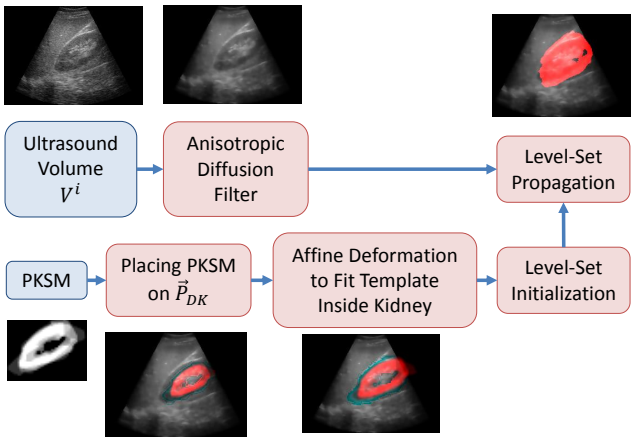

Fig. 3. Displaying the block diagram of our proposed kidney segmentation.

III. Results

We have implemented the proposed methods of kidney detection and kidney segmentation in MATLAB. We have utilized a database of 28 3-D ultrasound images, in which 14 volumes are correct Morison's pouch views with kidneys, and 14 volumes are randomly selected without kidneys. For the volumes with kidneys, ground truth data of their kidneys as binarized masks are manually generated. 4 binarized masks are used to generate PKSM, and the rest are used for evaluating our kidney segmentation.

Our proposed kidney detection method [20] is more sensitive to 2 parameters: the width of the Gaussian filter, N_{GH}, and the width of localized histogram equalization, N_L. We performed a parameter analysis using all 28 volumes to check different combinations of N_{GH} and N_L, which is shown in Fig. 4. The parameter analysis of N_{GH} and N_L can not be separately performed, since any change in the Gaussian filter parameter, N_{GH}, affects the localized intensity profile at each voxel, which influences the local histogram equalization performance. Based on the performed parameters analysis, we set $N_{GH} = 7$ and $N_L = 11$, aiming to minimize the detection error. Based on this settings, the detection accuracy is (#true positive detections + #true negative detections)/(#total number of detections)=92.86%.

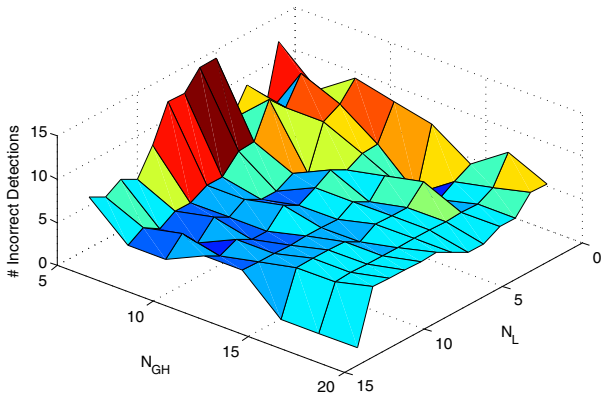

Fig. 4. Displaying parameters analysis of N_{GH} and N_L. The detection error for each combination of these two parameters are shown in the graph.

We have compared the kidney segmentation accuracy of our proposed method with MRF-AC [18], which is also developed in MATLAB. MRF-AC requires a manual intervention to fit the initial contour inside a kidney. To provide a fair comparison with our proposed approach, we substituted the manual intervention with our proposed automated PKSM alignment, discussed in section II-D. To perform the comparison, we excluded those 4 volumes which are used to create PKSM. Thus, the comparison is performed for 10 volumes, and the Dice's coefficient is used as the metric of calculating the segmentation accuracy. The kidney segmentation results are demonstrated in Table I. Accordingly, the average and standard deviation of kidney segmentation accuracies of our proposed method and MRF-AC are 0.6552 ± 0.0595 and 0.4691 ± 0.1026, respectively. The result of the paired t-test is $t = 7.6496$ and $p = 0.000032$, which strongly

confirms ($p < 0.01$) our proposed method provides a higher segmentation accuracy compared to MRF-AC. In addition to the segmentation accuracy, our proposed method outperforms MRF-AC since our proposed method provides a fully automated kidney segmentation approach, whereas MRF-AC requires manual intervention to fit the kidney shape model inside a kidney. Fig. 5 shows 2-D slices of two segmented kidneys.

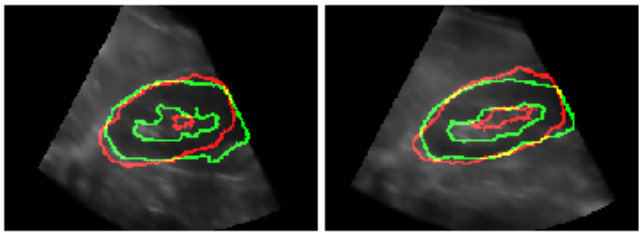

Fig. 5. Displaying two examples of kidney segmentation, in which 2-D slices are shown. Red lines show the automatically segmented kidneys, and green lines show manually segmented kidneys.

TABLE I

COMPARING KIDNEY SEGMENTATION RESULTS OF OUR PROPOSED METHOD WITH MRF-AC USING DICE'S COEFFICIENT.

#	MRF-AC	Our Proposed Approach
1	0.5032	0.6133
2	0.4337	0.6339
3	0.4610	0.6452
4	0.2414	0.6109
5	0.5347	0.7493
6	0.5014	0.7123
7	0.5820	0.6724
8	0.4508	0.6246
9	0.5940	0.7285
10	0.3893	0.5612

IV. CONCLUSION

In this paper, we proposed an approach to automatically detect and segment kidneys in 3-D abdominal ultrasound images. Our proposed kidney detection and segmentation methods are based on the probabilistic kidney shape model. We utilized 4 manually segmented kidneys to create the probabilistic kidney shape model. Our segmentation results confirm the superiority of our proposed method, compared to MRF-AC.

REFERENCES

[1] Stergios Stergiopoulos. Digital 3d/4d ultrasound imaging array. *Handbook on Array Processing and Sensor Networks*, pages 367–405, 2010.

[2] Stergiopoulos S. and Yi-Ting Shen. Portable 4d ultrasound diagnostic imaging system. Proceedings of IEEE UFFCS, 2011.

[3] A.C. Dhanantwari, S. Stergiopoulos, L. Song, C. Parodi, F. Bertora, P. Pellegretti, and A. Questa. An efficient 3d beamformer implementation for real-time 4d ultrasound systems deploying planar array probes. In *Ultrasonics Symposium, 2004 IEEE*, volume 2, pages 1421–1424, Aug 2004.

[4] A. Dhanantwari, S. Stergiopoulos, C. Parodi, F. Bertora, P. Pellegretti, and A. Questa. Adaptive 3d beamforming for ultrasound systems deploying linear and planar phased array probes. In *Ultrasonics, 2003 IEEE Symposium on*, volume 2, pages 1855–1858, Oct 2003.

[5] Jeff Powers and Frederick Kremkau. Medical ultrasound systems. *Interface focus*, 1(4):477–489, 2011.

[6] G. M. Treece. Volume measurement and surface visualisation in sequential freehand 3d ultrasound. (bl), 2001.

[7] K. Matsushima and H.L. Frankel. Beyond focused assessment with sonography for trauma: ultrasound creep in the trauma resuscitation area and beyond. *Curr Opin Crit Care*, 17(6):606–612, 2011.

[8] D. V. Feliciano B. D. Thomas B. R. Boulanger F. E. Davis R. E. Falcone J. A. Schmidt G. S. Rozycki, M. G. Ochsner. Early detection of hemoperitoneum by ultrasound examination of the right upper quadrant: A multicenter study. *The Journal of Trauma: Injury, Infection, and Critical Care*, 45(5):878–883, 1998.

[9] Yongjian Yu and S.T. Acton. Speckle reducing anisotropic diffusion. *Image Processing, IEEE Transactions on*, 11(11):1260–1270, 2002.

[10] A. Belaid, D. Boukerroui, Y. Maingourd, and J. F Lerallut. Implicit active contours for ultrasound images segmentation driven by phase information and local maximum likelihood. In *IEEE International Symposium on Biomedical Imaging: From Nano to Macro*, pages 630–635, 2011.

[11] B. Tsagaan, A. Shimizu, H. Kobatake, K. Miyakawa, and Y. Hanzawa. Segmentation of kidney by using a deformable model. In *International Conference on Image Processing, 2001*, volume 3, pages 1059–1062 vol.3, 2001.

[12] Baigalmaa Tsagaan, Akinobu Shimizu, Hidefumi Kobatake, and Kunihisa Miyakawa. *An Automated Segmentation Method of Kidney Using Statistical Information*, volume 2488. Springer Berlin Heidelberg, 01/01 2002.

[13] Daw-Tung Lin, Chung-Chih Lei, and Siu-Wan Hung. Computer-aided kidney segmentation on abdominal ct images. *IEEE Transactions on Information Technology in Biomedicine*, 10(1):59–65, 2006 JAN. 2006.

[14] Xinjian Chen and Ulas Bagci. 3d automatic anatomy segmentation based on iterative graph-cut-asm. *Medical physics*, 38(8):4610–4622, August 2011 2011.

[15] Ke Li and Baowei Fei. A new 3d model-based minimal path segmentation method for kidney mr images. In *Bioinformatics and Biomedical Engineering, 2008. ICBBE 2008. The 2nd International Conference on*, pages 2342–2344, 2008.

[16] Fahmi Khalifa, Ahmed Elnakib, GarthM Beache, Georgy Gimelfarb, MohamedAbo El-Ghar, Rosemary Ouseph, Guela Sokhadze, Samantha Manning, Patrick McClure, and Ayman El-Baz. *3D Kidney Segmentation from CT Images Using a Level Set Approach Guided by a Novel Stochastic Speed Function*, volume 6893, pages 587–594. Springer Berlin Heidelberg, 01/01 2011.

[17] Hamed Akbari and Baowei Fei. Automatic 3d segmentation of the kidney in mr images using wavelet feature extraction and probability shape model. pages 83143D–83143D, February 23 2012.

[18] Marcos Martin-Fernandez and Carlos Alberola-Lopez. An approach for contour detection of human kidneys from ultrasound images using markov random fields and active contours. *Medical image analysis*, 9(1):1–23, 2005.

[19] R. Prevost, B. Mory, J. Correas, L. D. Cohen, and R. Ardon. Kidney detection and real-time segmentation in 3d contrast-enhanced ultrasound images. In *Biomedical Imaging (ISBI), 2012 9th IEEE International Symposium on*, pages 1559–1562, 2012.

[20] P. Shek. K. Plataniotis S. Stergiopoulos and M. Marsousi. Computer aided diagnosis for detecting abdominal bleeding with 3d ultrasound imaging, us patent application 14/159,744, assignee:defence research and development canada,, 2014.

[21] John Ashburner and Karl J Friston. Rigid body registration. *Statistical parametric mapping: The analysis of functional brain images*, pages 49–62, 2007.

[22] Joung-Youn Kim, Lee-Sup Kim, and Seung-Ho Hwang. An advanced contrast enhancement using partially overlapped sub-block histogram equalization. *Circuits and Systems for Video Technology, IEEE Transactions on*, 11(4):475–484, 2001.

[23] D.J. Ketcham. Real-time image enhancement techniques. In *Image processing*, volume 74 of *Society of Photo-Optical Instrumentation Engineers (SPIE) Conference Series*, pages 120–125, 1976.

[24] W. Oh and W. B. Lindquist. Image thresholding by indicator kriging. *IEEE transactions on Pattern Analysis and Machine Intelligence*, 21(7):919–927, 1999.

[25] T. F. Chan and L. A. Vese. Active contours without edges. *IEEE Transactions on Image Processing*, 10(2):266–277, 2001.